Vacancy-induced flow of solid helium

Giorgio Benedek,[*] Anton Kalinin,[†] Pablo Nieto,[‡] and J. Peter Toennies
Max Planck Institut für Dynamik und Selbstorganisation, Am Fassberg 17, 37077 Göttingen, Germany
(Received 8 January 2015; revised manuscript received 22 January 2016; published 4 March 2016)

The pulsed flow of solid ^{4}He through a narrow capillary in a flow system which issues into vacuum is investigated at temperatures between 1.64 and 2.66 K and pressures between 54 and 104 bars. After each pulse three different capillary flow regimes are observed as the upstream pressure decreases: an oscillatory [mini-geyser (MG)] regime, a constant flow (CF) regime with a linearly decreasing pressure difference, and a nonresistant (NR) regime. A quantitative analysis of the three regimes suggests that the flow of solid ^{4}He is driven by a counterflow of excess vacancies, which are injected downstream of the capillary at the solid/liquid interface near the micrometric orifice exposed to vacuum. The CF regime, where the flow velocity is found to be independent of the pressure difference, and the NR regime, where the solid flows as a Bernoulli fluid, suggest a new dynamic phase of solid helium induced by a steady influx of vacancies.

DOI: 10.1103/PhysRevB.93.104505

I. INTRODUCTION

The predictions of Andreev and Lifshitz [1], Reatto and Chester [2], and Chiu and Chester [3] in the late 1960s that inherent vacancies in the otherwise perfect quantum ^{4}He solid at sufficiently low temperatures might Bose-Einstein condense into a superfluid state has in recent years led to renewed interest into this unusual phenomenon [4]. After eight years of active research down to milli-Kelvin temperatures the observations of superfluidity reported in 2004 [5–8] have been withdrawn and at the present time there is no conclusive evidence for the effect in well annealed crystals [7]. On the other hand, the torsional-oscillator experiments have motivated a great deal of experimental and theoretical work on defect-induced quantum superflow phenomena [8–12], in particular on superplasticity [13–17], where dislocations, due to their nonthermal nature, play the major role in the milli-Kelvin domain. For a very recent review see Hallock [12,18].

The present flow experiments are motivated by a study by Galli and Reatto in 2001 which showed through variational quantum Monte Carlo simulations that at a sufficiently high concentration of vacancies, another type of quantum condensation phenomenon might occur even at temperatures close to the lambda line (∼1.76 K) [19]. A subsequent more exact computation by the same authors [20] with a shadow path integral ground state (SPIGS) method, and quantum Monte Carlo calculations by Boronat and colleagues [21,22], confirmed the possibility of a vacancy-induced Bose-Einstein condensation (VIBEC). For a calculated effective vacancy mass of 0.35 × 4 amu Galli and Reatto predicted a critical temperature of $T_{\mathrm{BEC}} \sim 11.3 \cdot X_v^{2/3}$, where X_v is the vacancy concentration [23]. According to this prediction, a condensation at 1.6 K would require $X_v \sim 5\%$, which is much larger than the equilibrium vacancy concentration of about 0.5% at that temperature.

We are not presently aware of experiments which have tested these predictions possibly since it is, in fact, not straightforward to create a solid with such a high concentration of vacancies. In 2003 our group found that large *nonequilibrium* concentrations of excess vacancies could be achieved in pulsed vacuum expansions of solid He (*geyser effect*) [24–26]. In the expansion cell the blocked pressurized solid is exposed to vacuum via a small micron-sized orifice where vacancies are continually injected to compensate the pressure gradient. From the orifice region the vacancies propagate upstream causing the solid to gradually flow. Eventually they reach the upstream solid plug which had temporarily blocked the flow, thereby causing the plug to suddenly collapse. The released pulse of solid refills the cell and a new plug is formed. The process repeats itself indefinitely with a constant period of several 100 s which increases for increasing pressure or decreasing temperature [24–26].

To test the predictions of VIBEC we have investigated the pulsed vacancy induced flow of solid helium through a narrow capillary installed inside the same apparatus at temperatures T_0 between 1.64 and 2.66 K and initial pressures in the range $54 \leqslant P_0 \leqslant 104$ bars. Following the initial geyser pulse the flow of solid through the capillary is monitored upstream and downstream of the capillary by pressure sensors. After each pulse three different capillary flow regimes are observed as the upstream pressure decreases: an oscillatory [*mini-geyser* (MG)] regime, a *constant flow* (CF) regime with a linearly decreasing pressure difference, and a *nonresistant* (NR) regime. These flow regions are attributed to the oppositely directed flow of vacancies. Of special interest is the observation that in the CF regime the capillary flow has a relatively large velocity of between 21 and 28 cm s^{-1}, which is nearly *independent* of the decreasing applied pressure difference across the capillary and depends only weakly on temperature.

In the past the flow of solid helium has been studied only for small pressure differentials ($\Delta P \approx 0.2$ bar) at milli-K temperatures in closed systems. Two experiments reported a complete blockage [27,28], consistent with the *blocked*

[*]Present address: Donostia International Physics Center (DIPC) and University of the Basque Country (UPV-EHU), Paseo Manuel de Lardizábal 4, 20018 Donostia-San Sebastián, Spain, and Dipartimento di Scienza dei Materiali, Università di Milano-Bicocca, Via R. Cozzi 53, 20125 Milano, Italy.
[†]Present address: Institut für Kernphysik, J.W. Goethe-Universität, Max-von-Laue-Strasse 1, 60438 Frankfurt am Main, Germany.
[‡]Present address: Institut für Optik und Atomare Physik, Technische Universität Berlin, Hardenbergstrasse 36, 10623 Berlin, Germany.

capillary method [29] used for measuring the melting line. Only one experiment has succeeded in detecting an extremely slow flow of the solid at minute pressure differences and at low temperatures, $T < 600$ mK [11,30,31]. A comprehensive review of related experimental and theoretical flow studies has been presented in 2012 by Hallock, Ray, and Vekhov [31] and more recently by Hallock [12,18].

The present paper starts with a description of the apparatus and the experimental methods. Next, the time dependence of a typical geyser pressure pulse and the three flow regimes observed with a channel mounted inside the source are described and summarized in a temperature-pressure diagram. The steady state constant flow (CF) regime, which is characterized by a constant flux independent of the pressure difference across the capillary, is analyzed in detail. From the data the concentration of vacancies is estimated to be of the order of a few percent. The large measured solid helium velocity in the channel and its independence of the pressure difference cannot be explained classically nor with current theories. It is however consistent with very recent observations at much lower temperatures and very small pressure differences [32,33]. Here we argue that our observation might well be consistent with theoretical predictions of a vacancy induced type of BEC behavior.

II. APPARATUS

The apparatus (Fig. 1) is a modified molecular beam vacuum setup previously used to produce jets of liquid helium [34], which have since found important applications as a low-Z target in high energy nuclear collision studies [35]. When operated with solid helium the geyser effect was first observed in the same apparatus [24,25]. In the present

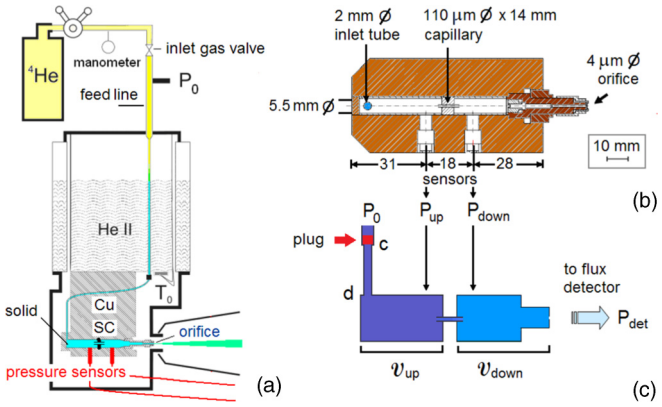

FIG. 1. (a) Schematic diagram of the cryostat and the He gas inlet and low-temperature flow system. Near the orifice the reduced pressure leads to melting thereby producing a beam of liquid which issues into a high vacuum system. There, an ionization gauge (not shown) measures the resulting pressure $P_{\rm det}$ and serves as a flux detector. (b) The source chamber (SC) showing the dividing wall and the capillary in the center of the cell. A laser-drilled micrometric orifice [38] with a diameter of $d_N = 3.93\,\mu$m connects the downstream cell to the vacuum system. The pressures in the two cells are measured with sensors flush with the cell wall. (c) The equivalent flow system showing the location of the upstream plug, the collapse of which initiates the main geyser pulse.

modification, as shown in Fig. 1(b), the evaporation-cryostat-cooled copper source chamber is divided by a 5-mm-thick copper wall into two cells. A stainless steel capillary [36] of length $l_{\rm ch} = 14.0$ mm and inner diameter $d_{\rm ch} = 110\,\mu$m connects the two cells. The pressures of the solid upstream and downstream of the capillary were monitored with two miniature quartz piezoelectric pressure sensors [37]. The sensors have a deviation from linearity of less than 0.2% full scale. Prior to each experiment they were calibrated by applying a known gas pressure. The temperature T_0 was measured at the copper bottom of the cryostat with a calibrated silicon diode [Fig. 1(a)].

The solid helium under pressure from the external supply of helium gas enters the upstream cell at its far end via the 2 mm inner diameter feedline (~ 5 cm^3 total volume below the average helium level). The downstream cell has a geometric volume $V_{\rm down} = 0.648$ cm^3. The effective volume of the upstream cell $V_{\rm up} = 1.291 \pm 0.04$ cm^3 is greater than the geometric volume since it includes the portion c-d of the inlet tube [0.471 cm^3, Fig. 1(c)] below the constriction c where the plug is known to form after each main geyser collapse [26]. This gives an effective total source volume $V_{\rm cell} = 1.94 \pm 0.04$ cm^3. At the other end of the downstream cell a laser drilled $d_N = 3.93\,\mu$m diameter thin walled orifice [38] connects the cell to the vacuum system. The latter is evacuated by two large turbo pumps with a total nominal helium pumping speed $S = 29001/s$ with a base pressure of 10^{-1} nbar (10^{-7} mbar) measured with an ionization gauge ($P_{\rm det}$) in the vacuum chamber. Throughout this article the pressure $P_{\rm det}$ is the pressure recorded by the ionization gauge. To obtain the true helium pressure $P^*_{\rm det}$, $P_{\rm det}$ has to be multiplied by a factor 5.

Since the flow of helium through the orifice raises the pressure in the external vacuum chamber by several orders of magnitude above the base vacuum pressure, $P_{\rm det}$ is directly proportional to the flux (expressed in mol/s) through the orifice via

$$j_{\rm out} = u_l s_N / V_l = S\, P^*_{\rm det} / R\, T_{\rm det}, \tag{1}$$

where u_l and V_l are the flow velocity and the molar volume of the liquid ^{4}He at the orifice, $s_N = \pi\, d_N^2/4 = 12.13 \times 10^{-8}$ cm^2 is the orifice cross section, $T_{\rm det}$ is the temperature of the detector vacuum chamber, and R is the gas constant.

As will be seen below, an important solid flow regime, called the constant flow (CF) regime, is observed in which the pressure in the downstream cell remains substantially constant and much above the melting pressure. In this case, assuming that *no change* of state occurs in the downstream cell, the flow through the channel remains constant by continuity, so that $j_{\rm out}$ provides a direct measure of the flow velocity $u_{\rm ch}$ in the capillary as given by

$$u_{\rm ch} \equiv u_{\rm CF} = j_{\rm out} V_0 / s_{\rm ch}, \tag{2}$$

where $s_{ch} = \pi d_{ch}^2/4 = 0.95 \times 10^{-4}$ cm^2 is the capillary cross section and V_0 is the molar volume of the flowing material.

Bernoulli's law relates the exit flux $j_{\rm out}$ to the pressure at the liquid/solid interface $P_{s/l}$ in the pressure fall-off region near the orifice [25,26]:

$$j_{\rm out} = s_N (2 P_{s/l} / V_l\, m_A)^{1/2}, \tag{3}$$

where $m_A = 4$ g/mol is the atomic weight of ^{4}He. When measured at the end of the main geyser period, where $P_{s/l}$ is approximately equal to the equilibrium melting pressure P_m, the flux values from Eqs. (1) and (3) agree within the experimental error. Thus, the ratio $j_{\rm out}/P_{\rm det}$, based on Eq. (3) and obtained from Eq. (1), both yield

$$j_{\rm out}/P_{\rm det} = 590 \pm 20 \ {\rm mol\,s^{-1}\,bar^{-1}}. \quad (4)$$

Within the same relative error, the flow velocity in the capillary is directly determined from the measured detector pressure $P_{\rm det}$. Thus, the apparatus allows the simultaneous measurement of both the time dependent flux through the capillary within $\pm 3\%$ and the pressures upstream and downstream of the capillary.

Since the effective cell volume $V_{\rm cell}$ is an important quantity in the interpretation of the data it was also measured directly via the continuity of flux. Accordingly, the effective cell volume $V_{\rm cell}$ times the change of the average molar density between the two well defined equilibrium states, for example, at t_0 (solid) and at τ_0 (liquid) [see Fig. 2(a)] must equal the measured ejected moles between the same two equilibrium states. For the geyser patterns discussed in this paper the value of $V_{\rm cell}$ derived in this way agrees with the effective value $V_{\rm cell} = 1.94\,{\rm cm}^3$ within $\sim 3\%$. Thus, as found in previous experiments without a capillary [26], the plug is located at the constriction c [Fig. 1(c)], where it completely blocks the flow without noticeable leakage over the entire geyser period.

It is important to note that according to Eq. (3) with each geyser pulse $P_{s/l}$ oscillates with $j_{\rm out}$ by a small amount with relative variations $\Delta P_{s/l}/2P_{s/l} \cong \Delta j_{\rm out}/j_{\rm out}$ which are proportional to those of the cell pressure [26]. Similarly, in the present setup the oscillations of $P_{s/l}$ follow those of the downstream pressure so that $\Delta P_{s/l}/P_{s/l} = \Delta P_{\rm down}/P_{\rm down}$. As a result, Bernoulli's law assures that the patterns of $P_{\rm det}$ and $P_{\rm down}-P_m$ are nearly identical, as is observed to within a few percent [see Figs. 2(a) and 2(c)]. This is consistent with previous experimental studies of the main geysers [26].

The experiments discussed in the present paper were all made under the above conditions. The relevant parameters for 27 selected experiments are listed in Table SM-I of the Supplemental Material [39]. A few experiments were also carried out with smaller orifices $d_N = 2\,\mu$m diameter and 1.44 μm diameter and a larger channel ($d_{\rm ch} = 180\,\mu$m, $l_{\rm ch} = 14.5$ mm). As it appears from the example

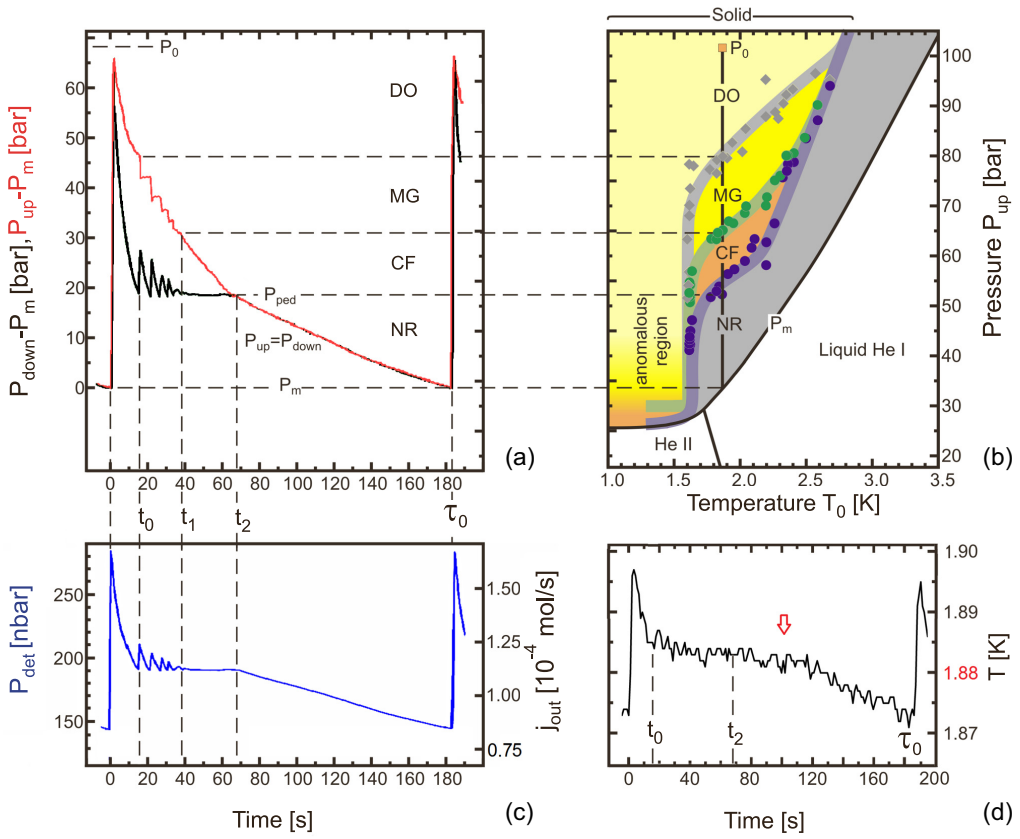

FIG. 2. (a) A typical mini-geyser pattern ($P_0 = 102$ bars, $T_0 = 1.88$ K, $P_m = 34$ bars) showing the upstream $P_{\rm up}(t)$–P_m and downstream $P_{\rm down}(t)$–P_m pressure profiles in red and black, respectively. The four main flow regimes are denoted as the *drop off* (DO) (from $t = 0$ to t_0), the *mini-geyser* (MG) (from t_0 to t_1), the *constant flow* (CF) (from t_1 to t_2), and *nonresistant (NR)* regimes (from t_2 to τ_0). (b) The vertical line shows a constant temperature cut through the pressure pattern in (a). The data points from 30 measurements exhibiting a CF regime, similar to (a), delineate the $P_{\rm up}$ pressure regimes projected onto the phase diagram of helium. (c) The detector pressure $P_{\rm det}(t)$ (left hand scale) and corresponding exit flux $j_{\rm out}(t)$ (right hand scale) profiles are close replicas of $P_{\rm down}(t)$–P_m for the geyser shown in (a). (d) The main amplitude of the cryostat temperature oscillations $T(t)$ is about 30 mK and has a shape similar to $P_{\rm down}(t)$ and $P_{\rm det}(t)$. The change of slope marked by the red arrow occurs where the effective molar volume of the solid becomes larger than the solid molar volume at melting [see Fig. 7(a)].

shown in Figs. SM-1(a) of the Supplemental Material [39], the signal has the same overall structure as discussed in the present paper, the major difference introduced by the use of smaller orifices being a change of time scale (roughly $\propto d_{ch}^{-2}$). Thus, the present analysis and conclusions also apply for smaller orifices. Figure SM-1(b) of the Supplemental Material shows a typical pressure pattern observed at temperatures below 1.57 down to 1.38 K.

III. EXPERIMENTAL RESULTS

A. Pulse shapes

The time profiles of all the four physical parameters which characterize a typical geyser-pulse-induced flow experiment are presented in Figs. 2(a), 2(c), and 2(d). Each pulse is part of a long sequence of pulses which are identical to within a few percent. Typical pressure and temperature profiles are discussed here and the flow regime diagram in Fig. 2(b) is discussed in the next section. A given experiment is completely characterized by only one geyser pulse which extends over a main geyser period τ_0, which is constant from one pulse to the next to within a few percent, and depends only on P_0 and T_0 [25,26]. In the example shown in Fig. 2; $P_0 = 102$ bars, $T_0 = 1.88$ K, $P_m = 34$ bars, and $\tau_0 = 182$ s. Figure 2(a) shows the pressures on both sides of the capillary in the upstream (red curve) and downstream (black curve) cells. The corresponding detector pressure profile (left hand ordinate scale) is shown in Fig. 2(c) together with the corresponding exit flux j_{out} (right hand ordinate scale) calculated using Eq. (1). Figure 2(d) shows the tiny temperature oscillations registered by the silicon diode at position T_0 (Fig. 1). The close similarity between the signals $P_{down} - P_m(t), P_{det}$, and $T(t)$ are discussed in detail below.

The initial sharp main geyser pulse is attributed to a sudden surge of solid material following the vacancy induced collapse of the plug of solidified helium in the feed line near the entrance to the source chamber [26]. The simultaneous and nearly equal initial pressure jumps in the upstream and downstream chambers and at the detector indicate that the highly fragmented solid passes through the channel and orifice into the vacuum system with virtually no resistance. The rapid drop-off, identified as DO in Fig. 2(a), following the initial sharp pressure pulse seen in the pressures both upstream and downstream of the capillary is attributed to the contraction accompanying recrystallization. This interpretation is further confirmed by the pressure difference $\Delta P = P_{up} - P_{down}$, which initially shows a large rapid increase indicative of a growing resistance of the capillary as the upstream material anneals to form larger crystals which eventually block the flow. In heterogeneous nucleation experiments Chavanne *et al.*, at the largest overpressures of 4.7 bars for which data are presently available, have observed growth of the crystals within 150 ns corresponding to a growth velocity of 100 m/s [40], which they claim holds for temperatures between 30 mK and 1.5 K [40]. Thus, in the following, we assume that at the end of the DO regime ($t = t_0$) the solid is completely recrystallized [see Fig. 2(a)] and in the equilibrium state.

At the end of the DO regime after about 20 s the decreasing upstream pressure P_{up} exhibits a sharp downward step ΔP_{up} while at the same time the downstream pressure P_{down} rises sharply. Similar correlated pressure changes are repeated with decreasing amplitude for about another 20 s. The series of downstream upward spikes ΔP_{down} are called *mini-geysers* [MG, Fig. 2(a)] due to their similarity to the main geysers [24–26]. The downstream pressure spikes are attributed to the sudden arrival of material from the upstream cell following the sudden collapse of a solid plug (mini-plug) at the entrance to the capillary. This is confirmed by the fact that the ratio $|\Delta P_{up}|/|\Delta P_{down}|$ for each pulse is equal to V_{down}/V_{up} within better than 10%. The complete but temporary blockage due to the mini-plug explains the constant pressure steplike plateaus in P_{up}. The constant upstream pressure is maintained until the vacancies which permeate through the channel from the downstream chamber reach a critical concentration leading to a collapse of the mini-plug. This behavior is completely analogous to the previous analyses of the main geyser pulses observed in the same apparatus under the same conditions but without the channel [26].

The mini-geyser downstream pressure spikes $\Delta P_{down}(n)$ $(n = 1,2,\ldots)$, and the P_{up} descending staircase steps $-\Delta P_{up}$ (n) exhibit a remarkably exact correspondence. At time intervals τ_n between the $(n+1)$th and the nth step, the ratio $\Delta P_{down}(n+1)/\Delta P_{down}(n)$ is equal to τ_{n+1}/τ_n within the statistical errors. An analysis of 18 mini-geyser sequences yields $\Delta P_{down}(n+1)/\Delta P_{down}(n) = 0.75 \pm 0.05$, to be compared with $\tau_{n+1}/\tau_n = 0.83 \pm 0.08$. The average ratio, which is denoted as α, is found to be independent of n. Thus the MGs form a self-similar exponential series with an endpoint at $\alpha\tau_1/(1-\alpha)$, entirely similar to that observed previously for the main geysers with the gas inlet valve closed [26]. This remarkable correspondence is further evidence for the reproducible creation of a completely perfect plug and the build-up of a reproducible critical concentration of vacancies needed for its collapse.

The downstream mini-geyser spikes are superimposed on a downstream nearly constant pressure plateau. The plateau, which is called the *pedestal* and denoted as P_{ped}, is also seen in the external detector signal P_{det}. The constant pressure of the plateau and the constant flux indicated by P_{det} means that material entering the downstream chamber via the mini-geyser pulses is fully compensated by the flux of liquid through the orifice. Note that for the measurement in Fig. 2, the pedestal is 20 bars above the melting pressure P_m and in all the experiments was invariably at a pressure well above the melting curve where He is definitely solid. Thus, the capillary flow can definitely not be attributed to the *melting* of the plug, but must be due to the repetitive collapse of a solidlike mini-plug formed at the entrance of the capillary. This can only be explained by the effect of the recurring accumulation of vacancies originating at the solid/liquid interface near the downstream orifice.

Beyond the MG endpoint [t_1 in Fig. 1(a)] the pedestal pressure P_{ped} continues to remain constant. At the same time $P_{up}(t)$ decreases smoothly with a constant slope. The constant values of P_{down} and P_{det}, despite the constant decrease in the pressure difference $\Delta P = P_{up} - P_{down}$, indicate, by continuity of flux, a constant flow of solid material through the capillary *independent* of the decreasing pressure difference between the upstream and the downstream cells. For this reason this is called the constant flow (CF) regime. Note that the preceding

MG oscillations may be viewed as quantized-steplike perturbations of the CF regime at the high pressures conducive to plug formation immediately after the drop-off.

Once P_{up} has become equal to P_{down} at $t_2 = 70\,s$ the flow enters into a new regime, the *nonresistant* (NR) regime, where the pressure profiles $P_{up}(t)$ and $P_{down}(t)$ cannot be distinguished, indicating that the capillary no longer resists the flow, which is only obstructed by the orifice. Both pressures decrease at a nearly constant rate indicating that both the chambers V_{up} and V_{down} are now simultaneously being drained of material. As a consequence the slope of $P_{up}(t)$ changes abruptly at $t = t_2$ from $\dot{P}_{up}(t_2^-) = j_{out} V_0^*/(\beta\, V_{up})$ at the left ($t \to t_2^-$) to $\dot{P}_{up}(t_2^+) = \dot{P}_{down}(t_2^+) = j_{out} V_0^*/(\beta\, V_{cell})$ at the right ($t \to t_2^+$) limit, where β is the compressibility. Since j_{out} and V_0^*, an effective molar volume, are still the same, the ratio $\dot{P}_{up}(t_2^-)/\dot{P}_{up}(t_2^+) = V_{up}/V_{cell}$ provides a check on the effective volume of the cell. The experimental ratio, averaged over 15 patterns which have a fully developed pedestal [$\dot{P}_{down}(t_1 < t < t_2) = 0$], is found to be 0.64 ± 0.04, which confirms the ratio $V_{up}/V_{cell} = 0.665$ obtained in Sec. II with the plug position at the constriction c of the feeding line [Fig. 1(c)]. This remarkable agreement supports the important conclusion that the flow in *both* the CF and NR regimes is limited only by the orifice. Otherwise the difference in the depletion rate of the upper cell would not be due exclusively to the change in the volume involved in the flow.

Finally, as discussed earlier [26], when the pressure in the entire cell equals the melting pressure the upstream plug at c in Fig. 1(c) is no longer able to withstand the applied pressure and the plug collapses thereby initiating the next main geyser. It is important to remark that the insertion of the capillary does not affect the regular recurrence of the main geyser effect over an indefinite number of periods. This demonstrates that also with the separation of the source chamber into two parts connected by a capillary the He is solid everywhere, except, of course, in the constriction near the orifice, and possibly at times very close to the next main geyser burst, when the pressure of the whole system approaches P_m.

Further support for the above interpretation comes from the temperature patterns, illustrated in Fig. 2(d). In general the temperature at the cryostat oscillates with a shape similar to P_{down} and P_{det}. The initial sharp pulse of about 0.03 K, which closely mimics the pressure pulse, is attributed to the heat burden from the new material entering the cryostat. In the subsequent constant temperature plateau the frictional power in the microchannel is very rapidly dissipated through the small He/steel interface Kapitza resistance [41]. A thermodynamic analysis of the system (see Appendix) shows that the resulting temperature rise of solid He is much less than the rise needed to produce melting. This important evidence definitely rules out that the flow through the channel is due to the formation of a liquid layer at the wall. The fact that the temperature signal reflects that of P_{down} and not that of P_{up}, indicates that most of the heat is released at the constriction near the orifice. It will be seen in Sec. IV that the change of slope of $P_{down}(t)$ at times beyond the arrow ($t \approx 105\,s$) in Fig. 2(d) occurs when the effective molar volume of the solid in the cell exceeds the solid molar volume at melting. However, beyond that point the temperature measured by the thermometer decreases below the cryostat temperature of $T_0 = 1.88\,K$ indicating a slight overcooling. The two observations together suggest that the liquid phase near the orifice starts encroaching into the cell subtracting latent heat from the thermostat.

B. The flow regime diagram

The reproducible characteristics of the upstream pressure pulses in Fig. 2(a) define the sharp borders of the four flow regimes. The *P,T* data marking the borders from 30 measurements have been superimposed on the (*P, T*)-phase diagram of solid helium in Fig. 2(b). The vertical line shows a constant temperature cut through the diagram at the temperature of 1.88 K corresponding to the upstream pressure pattern in Fig. 2(a). The boundaries in the phase diagram in Fig. 2(b) are derived from about 120 pressure profile measurements with the 3.93 μm orifice. Of these, Fig. 2(b) shows only the data points from 30 selected patterns most of which show an evident CF regime. The relevant parameters from an analysis of the 30 selected patterns are listed in Table SM-I of the Supplemental Material [39].

Figure 3 contains some of these patterns for decreasing temperatures at almost equal reservoir pressures $P_0 = 102$ and 104 bars in Figs. 3(a)–3(c), and for $P_0 = 95.5$ bars in Figs. 3(d)–3(f), and Fig. 4, for a fixed $T_0 = 1.64\,K$ and increasing P_0 [Figs. 3(a)–3(f)]. In general, with decreasing temperature T_0 the pressure signals P_{up} and P_{down}, which at the highest temperature of 2.2 K are indistinguishable, start to deviate from each other, then the first hint of a mini-geyser appears [Fig. 3(c)] and subsequently the constant flow regime characterized by a uniform decrease of P_{up} and constant P_{down} and P_{det} becomes fully developed [Fig. 3(f)]. However the temperature at which mini-geysers and a clear pedestal appear depends very much on the initial pressure P_0. A series of clearly delineated mini-geysers and a well-developed pedestal are generally obtained with larger reservoir pressures. This is clearly seen in Fig. 3 for the series [Figs. 3(d)–3(f)] and from the comparison of Fig. 3(a) with Fig. 3(d) and Fig. 3(b) with Fig. 3(e) taken at about the same T_0 and could possibly be due to a better recrystallization. A good recrystallization appears to be a precondition for the observation of mini-geysers and a well-defined CF regime. In any case beyond 2.4 K the boundaries delineating the CF regime converge indicating that it only occurs below this temperature [see Fig. 2(b)].

Only the extensive data above a critical temperature of $T_c = 1.57\,K$ is reported here. As observed previously for the main geysers [25,26,42] below this temperature the period suddenly shrinks and the signals become very sharp. The present capillary experiments show a similar transition. Below 1.57 K (in what we call *anomalous region*) the mini-geyser half-widths suddenly decrease and the pedestal pressure drops to values which are only a few bars above P_m. As shown in the example of Fig. SM-2(b) in the Supplemental Material [39], in other respects the pressure pulses in the anomalous region are essentially similar to those discussed here and exhibit similar MG, CF, and NR regimes. A discussion of the different behavior in the anomalous region and the mechanisms responsible for the differences will be presented in a forthcoming paper [43].

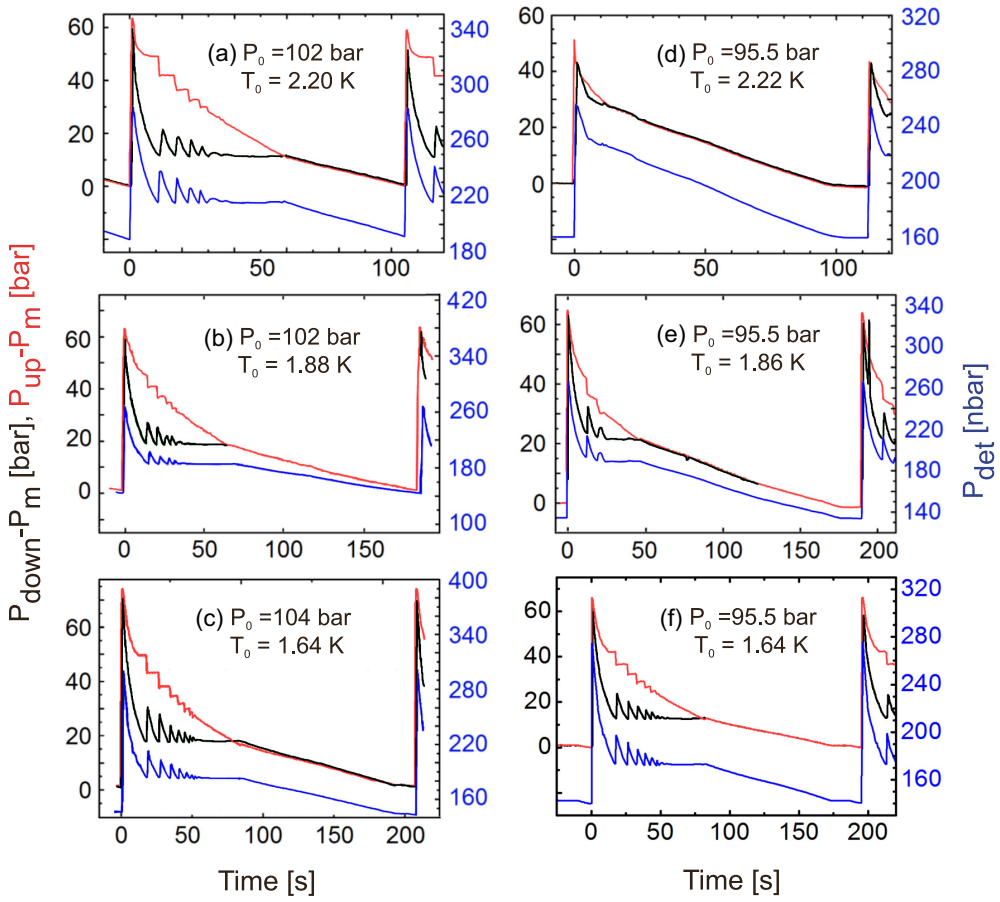

FIG. 3. A selection of time-dependent pressure profiles of $P_{\rm up}$ (upper red curve) and $P_{\rm down}$ (lower black curve) relative to the melting pressure P_m in the upstream and downstream chambers, respectively (left hand ordinate scale), and detector-pressure signals $P_{\rm det}$ (bottom blue curve, right hand ordinate). The series show the dependence of the patterns on decreasing temperature T_0 for reservoir pressures $P_0 = 102$ to 104 bars [(a)–(c)] and for $P_0 = 95.5$ bars[(d)–(f)]. At $P_0 = 95.5$ bars the pedestal with the MG and CF regimes starts being well defined only below about 1.9 K. At not much larger pressures (a)–(c) the pedestal with its MGs and the CF plateau are fully developed at T_0 as high as 2.20 K, but rapidly disappears at around 2.40 K [see Fig. 2(b)]. As in all the measurements, the initial spikes in Figs. 3 and 4 peak at the source pressure P_0. The corresponding melting pressures are listed in Table SM-1 [39].

C. The constant flow regime

In the following we discuss the implications resulting from the observation of an unexpected regime with constant flow independent of the pressure difference. Figure 5 shows some examples of $P_{\rm det}$ versus the measured pressure difference $\Delta P = P_{\rm up} - P_{\rm down}$ for four temperatures at $P_0 = 102$ and 104 bars. Equations (1) and (2) predict that the channel velocity $u_{\rm CF}$ for an assumed molar volume equal to the equilibrium molar volume V_0 [44] at the CF/NR transition point (see Table SM-1, column 13 [39]) is directly proportional to $P_{\rm det}$. As discussed in connection with Fig. 6 the presence of excess vacancies (see Sec. IV), or the choice of a molar volume in the range of ΔP has only an effect of a few percent. Thus, as seen in Fig. 5, the velocity in the CF regime u_{CF} (right hand ordinate) is about 21–26 cm/s which is surprisingly large. Both the velocity and the corresponding flux are nearly constant over the entire range of ΔP.

The observation of a constant flux of solid despite the steady fall-off of the upstream pressure is strikingly inconsistent with any known classical flow mechanism, whether for ideal fluids (Bernoulli regime) or viscous fluids (e.g., the Hagen-Poiseuille regime) [45,46]. The intriguing superplasticity properties of solid helium [13–17] which occur at much lower temperatures are not compatible with the present experiments. Also any surface stick-slip type of motion can be excluded for the same reasons, as discussed previously for the ordinary geysers (see Ref. [7] in [25]).

The constant flux phenomenon found here is surprisingly reminiscent of the flow observed by Allen and Miesener for superfluid He II in 1938 [47]. In their seminal article they reported that "the velocity of flow, q, changes only slightly for large changes in the pressure head, p." As discussed later this similarity may not be coincidental. A similar constant flow behavior of solid helium at much lower milli-Kelvin temperatures and much smaller pressure differences has also recently been reported [32,33].

Figure 6(a) presents the entire data for the flux $j_{\rm out}$ calculated from Eq. (4), and the channel velocity $u_{\rm CF}$ in the CF regime calculated from Eq. (2), both of which are listed in Table SM-I of the Supplemental Material [39]. Both show a small and almost linear increase with temperature, which is related via Eq. (3) to the increase of $P_{s/l} - P_m$. The five data

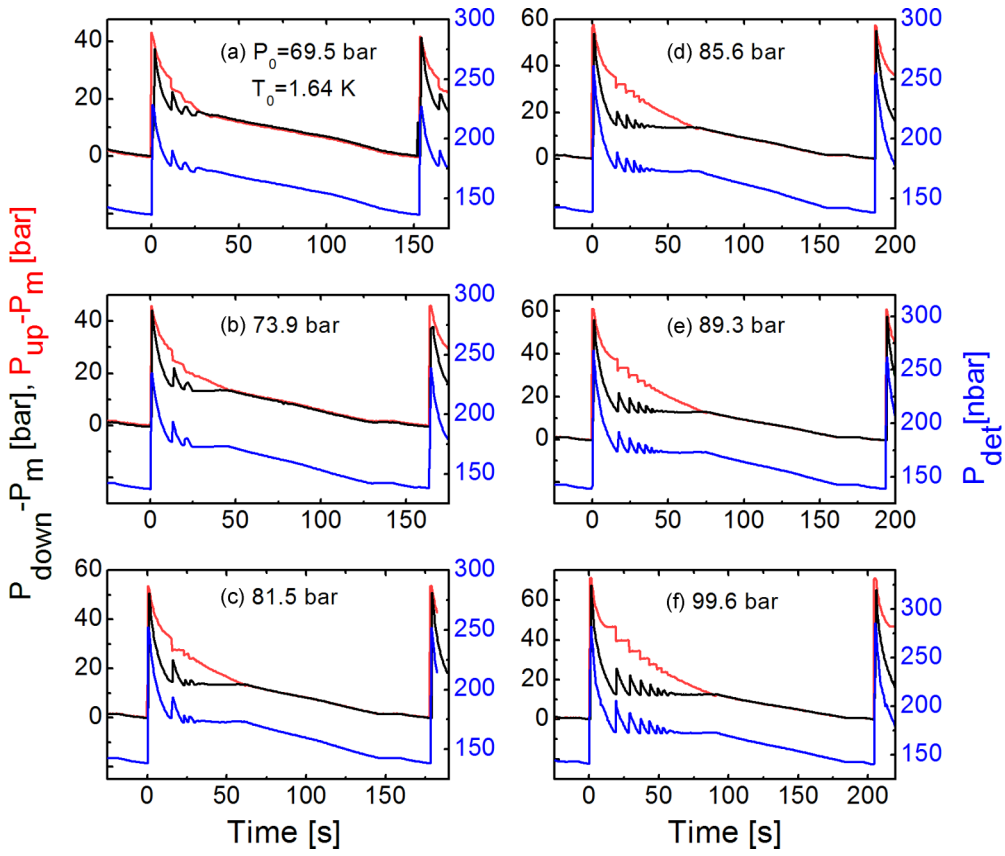

FIG. 4. A selection of time-dependent pressure profiles of P_{up} (upper red curve) and P_{down} (black curve) relative to the melting pressure $P_m = 27.87$ bars in the upstream and downstream chambers, respectively (left hand ordinate scale), and detector-pressure signals P_{det} (bottom blue curve, right hand ordinate). The series (a)–(f) shows the dependence of the patterns on increasing reservoir pressures P_0 at constant temperature $T_0 = 1.64$ K. The pedestal with the MG and CF regimes is fully developed only above about 70 bars. Note the gradual increase of the main geyser period with pressure and the proportional increase of the pedestal length. The same pressure patterns are nearly perfectly reproduced over an indefinite number of main geyser pulse cycles. Figures 3(c) and 3(f) also belong to this 1.64 K series.

points marked by the red vertical bars are for $P_0 > 100$ bars. The reservoir pressure dependence of the data in Fig. 6(a) at 1.64 K is displayed on an expanded scale in Fig. 6(b). The channel flow velocity (blue points) are calculated for the equilibrium molar volume u_{CF} (left hand ordinate) and for an effective molar volume V_0^*, which accounts for the presence of vacancies (see Sec. IV), denoted by u_{CF}^* (right hand ordinate). The latter are somewhat greater than u_{CF} by a few percent. Since the detector pedestal pressure at $T_0 = 1.64$ K is nearly independent of the pressure P_0 (see Table SM-I of the Supplemental Material [39]) j_{out} and also u_{CF} are also nearly the same for all patterns.

D. The nonresistant flow regime

In the NR regime the system behaves as in the ordinary geyser effect, as if no channel existed: the solid leaving the upper cell flows through the channel with no measurable resistance. One cannot avoid the conclusion that the solid He under the present flow conditions must be in some special phase. This phase, already responsible for the CF behavior, now extends throughout the entire source chamber. Additional insight into the nature of the solid in this phase comes from the slope of P_{down} in the NR regime, which can be used to determine the Poisson ratio ν. As discussed previously [48], the Poisson ratio in our apparatus is given by

$$\nu/(1-\nu) = \tfrac{1}{2} d \ln P_{down}/d \ln P_{det}, \quad (5)$$

where the slope on the right-hand side is obtained from the ratio of the time dependence of P_{down}, which is a measure of the stress on the wall, and the corresponding time change in P_{det}, which provides a measure of the longitudinal stress. The Poisson ratio ν averaged over the NR interval $\tau_0 - t_2$ for the patterns of Figs. 2(a) and 2(c) gives $\nu = 0.430 \pm 0.012$. This value is somewhat larger than the value of 0.41 reported earlier in geyser experiments at about the same pressure [48] and which has recently been confirmed for the solid in a theoretical study [49]. Nevertheless, it provides additional evidence that the material even at the lower pressures in the NR regime is definitely solid, the signature of an isotropic liquid being $\nu = 0.5$.

E. Data analysis

In the following the extensive results like those illustrated in Figs. 2 to 4 and collected in the Supplemental Material [39] are analyzed to provide information on the concentration and the possible influence of vacancies on the flow in the CF regime. The mechanism of generation and consequent accumulation of comparatively large concentrations of excess vacancies was

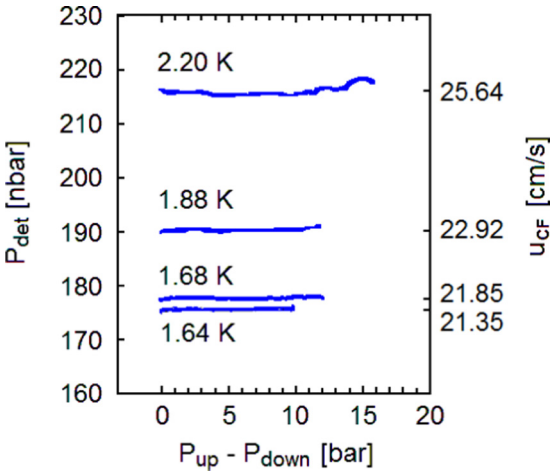

FIG. 5. Some typical measurements of P_{det} and the derived flow velocity u_{CF} versus the pressure difference $P_{up} - P_{down}$ between the upstream and downstream cells in the constant flow regime at $P_0 = 102$ bars for $T_0 = 2.20$ K ($P_{ped} = 57.2$ bars), 1.88 K ($P_{ped} = 52.26$ bars), 1.68 K ($P_{ped} = 45.33$ bars), and at $P_0 = 104$ bars for $T_0 = 1.64$ K ($P_{ped} = 44.38$ bars). The velocities u_{CF} (right hand ordinate) were calculated from continuity via Eqs. (1) and (2) for a molar volume assumed to be equal to the equilibrium molar volume V_0 at the CF/NR transition point (see Table SM-1, column 13 [39]). The presence of excess vacancies as discussed in Sec. IV leads to a few percent increase in the effective molar volume V_0^* (see Table SM-1, column 14 [39]) and correspondingly larger velocities. Choosing another molar volume between P_{up} and P_{down} would lead to less than a percent smaller velocities.

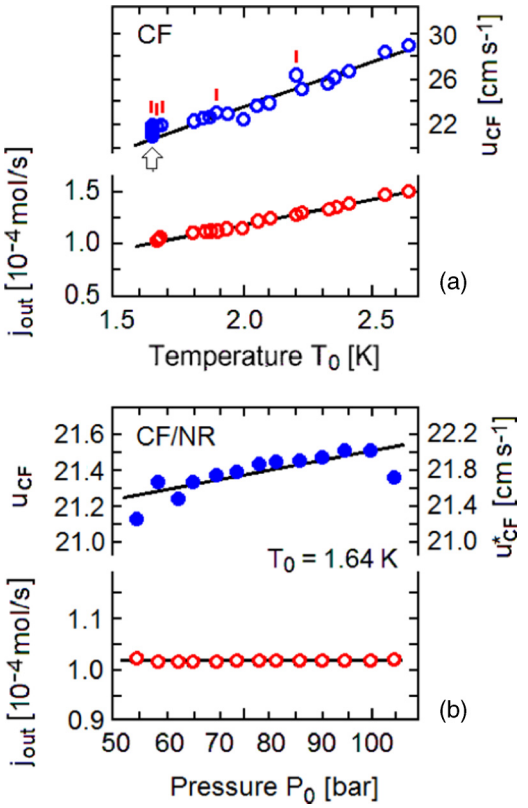

FIG. 6. (a) The temperature dependence of the flux j_{out} (left hand ordinate) and the channel flow velocity u_{CF} (right hand ordinate) in the CF regime for the 27 measurements listed in Table SM-I [39]. The spread of the u_{CF} data points with respect to the straight line fit reflects a slight dependence of u_{CF} on the pressure P_0. For example the five data points marked by vertical bars are for $P_0 > 100$ bars. (b) The reservoir pressure dependence of the flux (left-hand ordinate) and u_{CF} (left hand ordinate) at $T_0 = 1.64$ K for the measurements at this temperature (white arrow) in (a) and listed in the first 13 rows in Table SM-1 [39]. The values of u_{CF} are derived from Eq. (2) for the equilibrium CF/NR molar volume V_0 (Table SM-1, column 13 [39]. For effective molar volumes due to vacancies V_0^* (Table SM-1, column 14 [39]) the velocities u^*_{CF} are slightly greater by a few percent (right hand ordinate).

previously described for the main geyser effect [24–26]. In this scenario vacancies are generated and injected into the solid at the solid/liquid interface near the orifice where the pressure of the solid sharply drops from P_{down} to P_m from which point the pressure of the liquid drops down to the vacuum level [24–26]. Vacancies are readily generated at the solid/liquid interface since the reverse process of moving an atom from a solid site to a site in the liquid (available by continuity after the ejection of another atom into vacuum) is much easier than moving an atom from the solid into vacuum. At the solid/liquid interface the vacancy enthalpy increase $P_m[V_0^{liq}(P_m) - V_0^{sol}(P_m)]$ is only about $\sim$1 K, an order of magnitude less than the vacancy formation enthalpy. The vacancy injection process is in many respects analogous to the electric current through a p-semiconductor/metal contact under reverse bias, where hole (vacancy) - electron (atom) pairs are generated at the interface and excess (nonequilibrium) holes are injected into the p-semiconductor [50].

To estimate the vacancy concentration we take advantage of the increase of the molar volume due to the presence of vacancies, which leads to an increased effective molar volume V_0^*.

Our estimate is based on the assumption that, as discussed in Sec. III A, at the end of the drop-off regime at time t_0 [see Fig. 2(c)] the solid in both chambers has fully recrystallized. This is consistent with the repeated blockage of the flow through the channel by the solid mini-plugs at the entrance to the channel.

The vacancy induced increase in the mole volume from this point on can then be estimated by comparing the measured number of moles of helium $\Delta n(t) \equiv n(t_0) - n(t)$ which have left the system after a time $t - t_0$ with the number $\Delta n_{eq}(t)$ expected if the system would remain at equilibrium. $\Delta n(t)$ can be calculated by integrating $j_{out}(t)$ as obtained from P_{det} via Eq. (1). For the example of Fig. 2(a), the integration of $j_{out}(t)$ in the interval $t_2 - t_0$ gives $\Delta n(t_2) = 5.8 \times 10^{-3}$ mol.

Under equilibrium conditions Δn_{eq} would be equal to the change in the number of moles due to the decrease of pressure P_{up} and is given by

$$\Delta n_{eq} = V_{cell}\left[\bar{V}_0^{-1}(t_0) - V_0^{-1}(t_2)\right], \tag{6a}$$

where the average mole volume in the cell $\overline{V}_0$ is defined by

$$\bar{V}_0^{-1}(t) \equiv \frac{V_{\rm up} V_{0,\rm up}^{-1}(t) + V_{\rm down} V_{0,\rm down}^{-1}(t)}{V_{\rm cell}}. \qquad (6b)$$

The molar density in the upper cell $\bar{V}_{0,\rm up}^{-1}(t)$ decreases together with $P_{\rm up}$, while the lower cell is at the constant pedestal pressure apart from the small mini-geyser oscillations. For the example of Fig. 2 the equilibrium molar volumes at time t_0 are $V_{0,\rm up}(t_0) = 18.39\,{\rm cm}^3/{\rm mol}$, $V_{0,\rm down}(t_0) = 19.44\,{\rm cm}^3/{\rm mol}$, and $\bar{V}_0(t_0) = 18.73\,{\rm cm}^3/{\rm mol}$ [44]. At time t_2, since the pedestal pressure is the same in both cells, $\bar{V}_0(t_2) \equiv V_0(t_2) = V_{0,\rm down}(t_0)$. According to Eq. (6a) the number of ejected moles is 3.8×10^{-3} mol. Thus the effective average molar volume accounting for the observed emission of 5.8×10^{-3} mol is larger than the equilibrium value and equals $\bar{V}_0^*(t_2) = 19.85\,{\rm cm}^3/{\rm mol}$. This implies that an empty volume

$$\Delta V = V_{\rm cell}[1 - V_0(t_2)/\bar{V}_0^*(t_2)] \qquad (7)$$

has been introduced in the upstream volume and its most plausible form is that of vacancies. In general, the change with time of the average effective molar volume $\bar{V}_0^*(t)$ is related to the measured $\Delta n(t)$ by

$$\frac{\Delta \bar{V}_0^*(t)}{\bar{V}_0(t_0)} = \frac{\bar{V}_0^*(t)}{V_{\rm cell}} \Delta n(t) \cong \frac{\bar{V}_0(t)}{V_{\rm cell}} \Delta n(t). \qquad (8)$$

The above example is illustrated in Fig. 7(a) which shows the growth with time of $\Delta n(t)$ (left hand ordinate), as obtained from the integration of $j_{\rm out}(t)$, and of the corresponding $\bar{V}_0^*(t)$ (right hand ordinate). For comparison the broken green line shows the increase of the average equilibrium molar volume $\bar{V}_0(t)$ [Eq. (6b)]. It is important to note that this effective molar volume $\bar{V}_0^*(t)$ remains, however, below that of the solid at melting, $V_0^{\rm sol}(P_m) = 20.45\,{\rm cm}^3/{\rm mol}$ at $T_0 = 1.88\,{\rm K}$ up to about $t \approx 105\,{\rm s}$ [arrows in Figs. 2(d) and 7(a)]. Beyond this point the temperature measured by the thermometer decreases below T_0 [Fig. 2(d)] suggesting that the liquid, originally confined near the orifice, starts extending into the cell, subtracting latent heat from the system. At $t = \tau_0 = 180\,{\rm s}$, $\bar{V}_0^*(t)$ equals the liquid molar volume at melting $V_0^{\rm liq}(P_m)$: at this point $P_{\rm up} = P_{\rm down} = P_m(T_0)$, the main plug collapses leading to the next geyser burst.

Table SM-I column 14 [39] lists the effective average molar volume at time t_2 for 27 pressure patterns. The same data are plotted in Fig. 7(b) as a function of the pedestal time interval $t_2 - t_0$. During this time the vacancies accumulate in the cell and their final concentration increases almost linearly with the interval $t_2 - t_0$: actually the eye guideline in Fig. 7(b) suggests a smaller slope for shorter intervals $t_2 - t_0$. This can be explained by noting that shorter pedestals occur for smaller reservoir pressures P_0, at which recrystallization is less complete with many residual defects yielding a shorter vacancy annihilation lifetime.

The molar concentration $X_v(t_2)$ of excess vacancies accumulated at the end of the CF regime ($t = t_2$) in the whole cell volume is given by

$$X_v(t_2) = \frac{\Delta V}{\upsilon_v V_{\rm cell}}, \qquad (9)$$

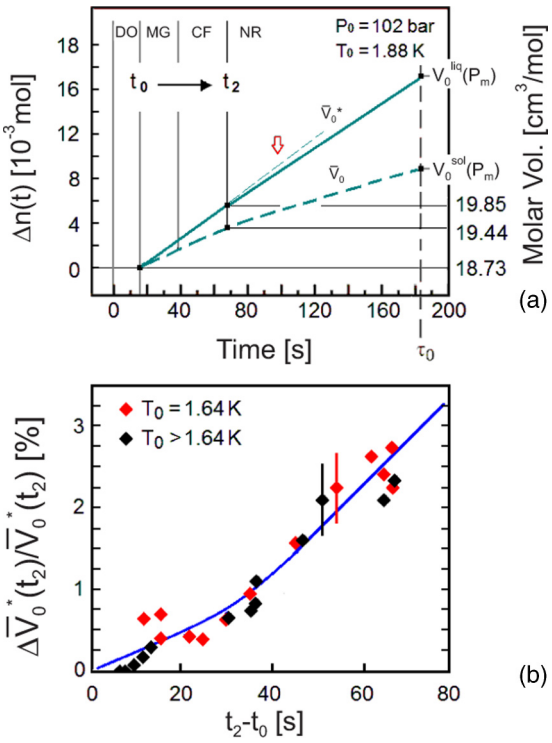

FIG. 7. (a) The cumulative loss of material from the entire source chamber $\Delta n(t)$ in the experiment shown in Fig. 2 (solid line) is plotted on the left hand ordinate scale as a function of time $t - t_0$, where t_0 marks the end of the DO regime [Fig. 2(c)]. $\Delta n(t)$ is obtained by integrating the flux into the vacuum chamber over time. The small kinks produced by MGs in $\Delta n(t)$ are not perceptible on the present scale. The thin broken line for $t > t_2$ shows a linear increase, while the actual slope decreases slightly beyond t_2. The corresponding average effective molar volume $\bar{V}_0^*$ (solid line) is given in the right hand ordinate scale and compared to the average equilibrium molar volume $\bar{V}_0$ of the solid in the entire source chamber (broken thick line). The equilibrium molar volumes of the solid and the liquid at melting are also indicated. Beyond the time marked by the red arrow $\bar{V}_0^*$ exceeds $V_0^{\rm sol}(P_m)$. (b) The relative increase of the effective average molar volume at time t_2, corresponding to the excess vacancy concentration, for the patterns listed in Table SM-I [39]. The eye guideline (full curve) suggests a smaller slope at smaller $t_2 - t_0$, i.e., for smaller P_0, which can be attributed to a shorter vacancy annihilation lifetime.

where $\upsilon_v = V_v/V_0(t_2)$ is the ratio of the vacancy formation molar volume V_v to the solid molar volume. Since presently the vacancy volume is not well known the results are reported in terms of $X_v^0(t_2) \equiv \upsilon_v X_v(t_2)$. With Eqs. (8) and (9) $X_v^0(t_2)$ can be expressed in terms of measurable quantities:

$$X_v^0(t_2) = 1 - V_0(t_2)/\bar{V}_0^*(t_2). \qquad (10)$$

Estimations of υ_v from x-ray measurements by Fraass *et al.* [51], as well as from shadow-wave-function variational studies by Pederiva *et al.* [52] indicate that V_v is somewhat smaller (say of ~25%) than the equilibrium molar volume due to inward relaxation. Calculations at $T = 0\,{\rm K}$ by Lutshyshyn *et al.* [53] indicate for pressures in the range of the present $P_{\rm ped}$ values of the vacancy formation molar volume of about the bulk molar volume. Note however that in the vacancy

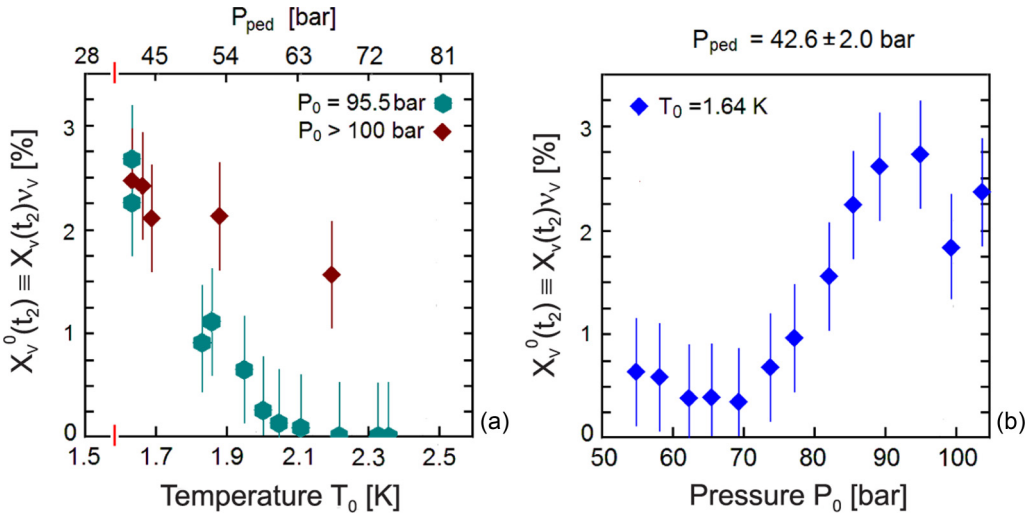

FIG. 8. (a) $X_v^0(t_2)$, the product of the excess vacancy concentration $X_v(t_2)$ and the relative vacancy molar volume υ_v, at the end of the constant flow regime ($t = t_2$) in the upstream cell as a function of temperature (lower abscissa) and of the pedestal pressure (upper abscissa) as derived from Eq. (10) for two different reservoir pressures P_0: red diamonds 102–104 bars and blue hexagons 95.5 bars pressure. The vertical red bars on the abscissas mark the onset of the anomalous region. (b) Same as (a) but as a function of the reservoir pressure P_0 for constant $T_0 = 1.64$ K. In this case the pedestal pressure is about the same (42.6 ± 2.6 bars) for all the measurements.

model of the geyser effect [24,25] υ_v needs to be <1 in order to have vacancies climbing the pressure gradient.

Figure 8(a) shows some typical values of $X_v^0(t_2)$ as a function of temperature for $P_0 = 102$–104 bars and at $P_0 = 95.5$ bars. At low temperatures the vacancy concentrations are about the same but surprisingly the vacancy concentration at higher temperatures are larger at $P_0 > 100$ bars. Below about 1.8 K the vacancy concentrations (assuming $\upsilon_v \cong 1$) are about one order of magnitude larger than the equilibrium concentration, and about 2%, the value at which the path integral Monte Carlo simulations of Clark and Ceperley indicated that the system collapsed into a liquidlike phase [54]. As seen in Fig. 8(b) at $T_0 = 1.64$ K the excess vacancy concentration decreases with decreasing reservoir pressure P_0. The larger vacancy concentration at high pressures can be explained by the larger accumulation time, which is proportional to $t_2 - t_0$ and which increases with P_0 [25]. In this connection it is important to note that the exit flux is practically independent of P_0 (see Table SM-I [39]). In addition we argue, based on these observations, that at higher pressures the recrystallization is more perfect so that the number of defects available for annihilating vacancies is much less.

IV. DISCUSSION

As for the ordinary geysers, the present experiments with a capillary reveal a new phenomenon called *mini-geysers*. While the main geysers exhibit the same perfect periodicity over a nearly unlimited number of periods as in the ordinary geyser effect, the mini-geysers show self-similarity as found in the corresponding closed-valve main geyser experiments [26]. The regularity of the geyser pulses and their occurrence under a wide range of conditions as shown here is viewed as further evidence that coherent macroscopic processes involving vacancies and mobile atoms must be governing both phenomena.

The involvement of vacancies in the flow of a quantum solid at temperature and pressure conditions where thermal vacancies have a sufficiently high concentration seems to be well established. In devising a new method to inject impurities into solid He, Gordon *et al.* [55] have observed that the solid can flow inside a cylinder cell as a whole with negligible friction at the cell wall, even at temperature as low as 1.4 K and a small pressure gradient. These authors attribute the flow of quantum crystals of helium (and also of hydrogen) to the high vacancy mobility [55]. Indeed at equilibrium concentrations in the present range of temperature and pressure, vacancies have been shown to drift with a comparatively high mobility under a linear friction [56,57]. The present study illustrates how the quantum solid helium is able to flow in the presence of a high and controlled concentration of excess vacancies. Under these conditions the flow in the downstream cell is observed to follow a frictionless (Bernoulli) flow regime at all times, except in the drop-off (recrystallization) region. The vacancy model implies also that the counterflow of excess vacancies at a sufficiently high concentration follows the Bernoulli regime, at least within the accuracy of the present pressure measurements. A nearly frictionless motion sets in when the excess vacancy concentration exceeds several percent and is more than an order of magnitude greater than the equilibrium value of about 1.5×10^{-3} in the same temperature range [51].

The large concentration of vacancies has important implications for the interpretation of the velocity u_{CF} measured in the constant flow regime. If only atoms and no vacancies were involved in the flow then the velocities inside the capillary would be the observed velocities u_{CF} of 20 to 30 cm s^{-1} (Fig. 5). On the other hand, if the mass flow is exclusively due to a counterflow of vacancies inside a bulk solid at rest, then the vacancies must move upstream at a substantially larger velocity $|u_v| = u_{CF}/X_v$, where X_v is the (excess + equilibrium) vacancy concentration inside the channel: for example for $X_v = 2\%$ the vacancy upstream velocity u_v would

be 10 to 15 m/s. In the general case where the flow consists of both a slow downstream bulk atom component (velocity $u_{\rm bulk}$) and a fast upstream vacancy component the velocity is given by $u_{\rm CF} = X_v|u_v| + (1 - X_v)\,u_{\rm bulk}$. This partition needs to be considered also in the case that the bulk flow of atoms is involved due to the superplasticity effects discussed in Refs. [12–17]. In this more general situation u_v would also be of the order of 10–15 m/s provided that $u_{\rm bulk}$ is significantly less than $u_{\rm CF}$. Note however that also a velocity of between 20 and 30 cm s^{-1} is far greater than expected if the plastic flow is assisted by dislocations and/or vacancies as in the Nabarro-Herring mechanism for high vacancy concentrations [58,59]. It is also much greater than the velocity due to the ordinary drift of vacancies under the pressure gradients of the experiments, which are estimated to be in the range of 10^{-3} cm/s [25].

Thus we conjecture that the flow might possibly be related to a type of quantum effect such as vacancy induced Bose-Einstein condensation (VIBEC). This is reasonably consistent with the work of Galli and Reatto [19,20,23] and several other recent quantum many-body simulations [21,22,60] which predict a Bose-Einstein condensation temperature T_c for the solid with a large vacancy concentration. The estimates differ widely, depending on what is assumed for the effective mass of the vacancies. For a vacancy concentration of 1% and 2%, values for T_c of 0.52 and 0.83 K [20], or 0.57 and 1.69 K [21], respectively, can be calculated from the reported vacancy dependence of T_c on vacancy concentration. These temperatures are also consistent with the disorder-induced anomalies at temperatures below about 1.8 K observed by Eyal *et al.* [61] in torsion oscillator experiments. In a theoretical investigation Kwang-Hua attributed these effects to a sharp drop in the shear stress by three orders of magnitude in an *amorphous* solid at about the same temperature [62]. On the other hand, experiments by Haziot *et al.* have experimentally demonstrated a giant plastic behavior in ultrapure solid ^{4}He at lower temperatures (∼0.2 K) [13]. The above results are also consistent with the finding of Clark and Ceperley [54] that the solid collapses into a liquidlike phase when the vacancy concentration reaches 2%.

As far as we are aware, there has been only one estimate of *velocities* due to superflow under the conditions of our experiments which is due to Rica [63]. His estimate is based on a phenomenological Ginzburg-Landau theory for superfluidity in the solid phase, according to which the critical velocity of the superfluid component is given by $u_c = (2\Pi_3 k_B T_c/m)^{1/2}$. With the dimensionless parameter $\Pi_3 = 3.6 \times 10^{-3}$ derived for He in aerogel, $T_c \sim 2$ K, and m equal to the He atomic mass, one finds $u_c \sim 5.7$ m/s.

In conclusion the pulsed flow experiments reported here indicate that under steady-state nonequilibrium conditions, in a flow system issuing into vacuum, solid helium at pressures between 54 and 102 bars and temperatures between 1.64 and 2.66 K the solid can sustain a type of nearly frictionless flow with a large velocity between 21 and 30 cm s^{-1} largely independent of the pressure difference over a wide range of pressures. Evidence is presented that the nearly constant flow can be explained by the injection of excess vacancies of several percent into the solid at the solid/liquid interface connecting the system to a vacuum. The results support the conjecture that the phenomenon might be due to some type of quantum condensation. Since the vacancy concentration attains values at which according to Clark and Ceperley's simulations [54], the solid should exhibit a liquid-like behavior, it is possible that the observed flow phenomena is associated to this new phase of solid helium.

ACKNOWLEDGMENTS

We acknowledge many illuminating discussions with Davide Galli (University of Milano, Italy), Sebastien Balibar (Ecole Normale Supérieure, Paris), and Anatoly B. Kuklov (CUNY, US). We thank Massimo Boninsegni, Robert Grisenti, and Yaroslav Lutsyshyn for correspondence and comments and Sascha Warnecke for technical assistance. G.B. acknowledges the Alexander-von-Humboldt Stiftung for support. P.N. thanks the Institute IMDEA Nanoscience (Madrid) for financial support.

APPENDIX

To estimate the temperature increase at the cryostat [see Fig. 1(a)] we have used the thermal resistance for the solid He/solid copper interface (Kapitza resistance) at the temperatures between 1 and 2 K as given by [41,64]

$$R_T \cong 6.6 T^{-3}\ \mathrm{K^4\,cm^2/W}. \tag{A1}$$

For the liquid ^{4}He/iron interface (applicable to the channel wall) a further ∼50% reduction is reported with respect to copper (see Fig. 18 in Ref. [64]), and a similar reduction is expected for solid ^{4}He. Thus, the above value is taken as an upper limit for the solid He interfaces in our apparatus at present experimental temperatures and pressures.

The *power dissipated* through the walls of the channel (lateral surface $s_l = 0.048\,\mathrm{cm^2}$), assuming a heating of the solid inside the channel of 0.5 K [the temperature rise needed to reach melting at the pressure of $P_{\rm ped}$ in the example of Fig. 2(a)] at $T_0 = 1.88$ K is given by

$$W_{\rm out} = \frac{\Delta T}{R_T} s_l = \frac{0.5\ \mathrm{K} \cdot 0.048\ \mathrm{cm^2}}{6.6\ K^4\,\mathrm{cm^2}} (1.88\ \mathrm{K})^3\ \mathrm{W} = 24\ \mathrm{mW}. \tag{A2}$$

This power, to be considered a lower limit, largely exceeds the *power produced* by the channel flow (cross section $s_{\rm ch} = 0.95 \times 10^{-4}\,\mathrm{cm^2}$, velocity $u_{\rm CF} = 24$ cm/s, maximum pressure difference at the onset of the ($P_{\rm up}$–$P_{\rm down} = 11$ bars) as given by

$$W_{\rm in} = u_{CF}(P_{\rm up} - P_{\rm down}) s_{ch} = 2.46\ \mathrm{mW}. \tag{A3}$$

Thus, the heating in the channel is a factor 10 less than $W_{\rm out}$ and melting is not possible.

The thermal relaxation time through the source chamber walls (total area $s_{\rm wall} = 13\,\mathrm{cm^2}$) is given by

$$\tau_r = C R_T / s_{\rm walls}, \tag{A4}$$

where the volume heat capacity C has two contributions: one from the helium in the cell C_{He} and another from the copper support C_{Cu}. The former is given by

$$C_{\mathrm{He}} = \frac{12\pi^4}{5} R \left(\frac{T}{\theta_D}\right)^3 \frac{V_{\mathrm{cell}}}{V_0} = 0.055 \ \frac{\mathrm{J}}{\mathrm{K}}, \qquad \text{(A5)}$$

where R is the gas constant, $\theta_D = 25\,\mathrm{K}$ is the Debye temperature of the solid, V_0 is the solid molar volume, and $V_{\mathrm{cell}} = 1.94\,\mathrm{cm}^3$ is the source chamber volume. This alone gives $\tau_r = 9.2\,\mathrm{ms}$. Thus, the relaxation time exclusively due to the Kapitza resistance is very short, which explains the observed simultaneity of the temperature and pressure signals. For bulk copper the heat capacity contains also the free electron contribution [65]

$$C_{Cu} = \left[\frac{12\pi^4}{5} R \left(\frac{T}{343}\right)^3 + 0.695 \times 10^{-3} \frac{\mathrm{J}}{\mathrm{mol\,K}^2} T\right] \times \frac{V_{\mathrm{Cu,block}}}{V_{0,Cu}} = 1.37 \times 10^{-3} \frac{\mathrm{J}}{\mathrm{mol\,K}} \frac{V_{\mathrm{Cu,block}}}{V_{0,Cu}}, \qquad \text{(A6)}$$

with $V_{0,\mathrm{Cu}} = 7.11\,\mathrm{cm}^3\,\mathrm{mol}^{-1}$. For a ratio $V_{\mathrm{Cu,block}}/V_{0,\mathrm{Cu}} \sim 10$ the heat capacity of the copper block is however less than that of solid He. Thus, the temperature changes detected by the thermometer should be only somewhat reduced with respect to those occurring in the solid He, despite the distance. However, when solid/liquid coexist in the terminal part of the NR regime and the He temperature inside the chamber remains constant, the slight drop of the thermometer temperature signals the latent heat absorption.

[1] A. F. Andreev and I. M. Lifshitz, Zh. Eksp. Teor. Fiz. **56**, 2057 (1969) [Sov. Phys. JETP **29**, 1107 (1969)].
[2] L. Reatto and G. V. Chester, Phys. Rev. **155**, 88 (1967).
[3] V. Chiu and G. V. Chester, Phys. Rev. A **1**, 1549 (1970).
[4] M. H. W. Chan, R. B. Hallock, and L. Reatto, J. Low Temp. Phys. **173**, 354 (2013).
[5] E. Kim and M. H. W. Chan, Nature (London) **427**, 225 (2004).
[6] E. Kim and M. H. W. Chan, Science **305**, 1941 (2004).
[7] D. Y. Kim and M. H. W. Chan, Phys. Rev. Lett. **109**, 155301 (2012)
[8] E. Burovski, E. Kozik, A. Kuklov, N. Prokof'ev, and B. Svistunov, Phys. Rev. Lett. **94**, 165301 (2005).
[9] M. W. Ray and R. B. Hallock, Phys. Rev. Lett. **100**, 235301 (2008).
[10] M. W. Ray and R. B. Hallock, Phys. Rev. B **79**, 224302 (2009).
[11] M. W. Ray and R. B. Hallock, Phys. Rev. B **84**, 144512 (2011).
[12] R. B. Hallock, J. Low Temp. Phys. **180**, 6 (2015).
[13] A. Haziot, X. Rojas, A. D. Fefferman, J. R. Beamish, and S. Balibar, Phys. Rev. Lett. **110**, 035301 (2013).
[14] M. Boninsegni, A. B. Kuklov, L. Pollet, N. V. Prokof'ev, B. V. Svistunov, and M. Troyer, Phys. Rev. Lett. **99**, 035301 (2007).
[15] L. Pollet, M. Boninsegni, A. B. Kuklov, N. V. Prokof'ev, B. V. Svistunov, and M. Troyer, Phys. Rev. Lett. **101**, 269901(E) (2008).
[16] S. G. Soyler, A. B. Kuklov, L. Pollet, N. V. Prokof'ev, and B. V. Svistunov, Phys. Rev. Lett. **103**, 175301 (2009).
[17] A. B. Kuklov, L. Pollet, N. V. Prokof'ev, and B. V. Svistunov, Phys. Rev. B **90**, 184508 (2014).
[18] R. Hallock, Phys. Today **68**, 30 (2015).
[19] D. E. Galli and L. Reatto, J. Low Temp. Phys. **124**, 197 (2001).
[20] D. E. Galli and L. Reatto, Phys. Rev. Lett. **96**, 165301 (2006).
[21] R. Rota and J. Boronat, Phys. Rev. Lett. **108**, 045308 (2012).
[22] R. Rota, Y. Lutsyshyn, C. Cazorla, and J. Boronat, J. Low Temp. Phys. **168**, 150 (2012).
[23] D. E. Galli and L. Reatto, Phys. Rev. Lett. **90**, 175301 (2003).
[24] G. Benedek, R. Grisenti, J. P. Toennies, and F. Dalfovo, J. Electron. Spectrosc. **129**, 201 (2003).
[25] G. Benedek, F. Dalfovo, R. E. Grisenti, M. Kasz, and J. P. Toennies, Phys. Rev. Lett. **95**, 095301 (2005).
[26] G. Benedek, P. Nieto, and J. P. Toennies, Eur. Phys. J. B **76**, 237 (2010).
[27] D. S. Greywall, Phys. Rev. B **16**, 1291 (1977).
[28] J. Day, T. Herman, and J. Beamish, Phys. Rev. Lett. **95**, 035301 (2005).
[29] C. A. Swenson, Phys. Rev. **89**, 538 (1953).
[30] Y. Vekhov and R. B. Hallock, Phys. Rev. Lett. **109**, 045303 (2012).
[31] R. B. Hallock, M. W. Ray, and Y. Vekhov, J. Low Temp. Phys. **169**, 264 (2012).
[32] Z. Cheng and J. Beamish (private communication).
[33] B. Hallock, mentioned in invited talk at QFS, August 2015.
[34] R. E. Grisenti and J. P. Toennies, Phys. Rev. Lett. **90**, 234501 (2003).
[35] M. Kuhnel, N. Petridis, D. F. A. Winters, U. Popp, R. Dörner, T. Stohlker, and R. E. Grisenti, Nucl. Instrum. Methods A **602**, 311 (2009).
[36] S. Zefa Laborservices GmbH, 85630 Harthausen, Germany.
[37] High pressure quarz sensor type 601 A, Kistler Instruments, Switzerland.
[38] National Aperture Inc, 16 Northwestern Drive, Salem, NH 03079, USA.
[39] See Supplemental Material at http://link.aps.org/supplemental/10.1103/PhysRevB.93.104505 for a collection of the relevant parameters and the data of 27 selected experiments for temperatures between 1.64 and 2.66 K and pressures between 54 and 104 bars (Table SM-I). In addition exemplary pressure patterns are shown for an experiment with a smaller orifice, and an experiment at a lower temperature of 1.44 K [Fig. SM.1(a,b)]. In both cases the same distinct MG series and CF regimes are clearly seen.
[40] X. Chavanne, S. Balibar, and F. Caupin, Phys. Rev. Lett. **86**, 5506 (2001).
[41] L. P. Mezhov-Deglin, Zh. Eksp. Teor. Fiz. **71**, 1453 (1976) [Sov. Phys. JETP **44**, 761 (1976)].
[42] G. Benedek, R. E. Grisenti, M. Käsz, and J. P. Toennies, J. Low Temp. Phys. **146**, 393 (2007).

[43] G. Benedek, A. Kalinin, P. Nieto, and J. P. Toennies (unpublished).
[44] A. Driessen, E. van der Poll, and I. F. Silvera, Phys. Rev. B **33**, 3269 (1986).
[45] A simple calculation shows that the flow cannot be due to that of a pressurized liquid. The viscosity of liquid He has been measured by Tjerkstra [46] at 40–50 bars and 2.20 K to be 120×10^{-6} P. The Hagen-Poiseuille law pressure drop for a flow of 10^{-4} mol/s (see Table SM-I [39]) is about 10^{-3} bar, which is more than three orders of magnitude less than observed.
[46] H. H. Tjerkstra, Physica **18**, 853 (1952).
[47] J. F. Allen and A. D. Misener, Nature (London) **141**, 75 (1938).
[48] P. Nieto, G. Benedek, and J. P. Toennies, New J. Phys. **14**, 013007 (2012).
[49] A. Grechnev, S. M. Tretyak, Y. A. Freiman, A. F. Goncharov, and E. Gregoryanz, Phys. Rev. B **92**, 024102 (2015).
[50] C. M. Wolfe, N. Hoonyak, and A. Stillman, *Physical Properties of Semiconductors* (Prentice Hall, New York, 1989).
[51] B. A. Fraass, P. R. Granfors, and R. O. Simmons, Phys. Rev. B **39**, 124 (1989).
[52] F. Pederiva, G. V. Chester, S. Fantoni, and L. Reatto, Phys. Rev. B **56**, 5909 (1997).
[53] Y. Lutsyshyn, C. Cazorla, and J. Boronat, J. Low Temp. Phys. **158**, 608 (2010).
[54] B. K. Clark and D. A. Ceperley, Comput. Phys. Commun. **179**, 82 (2008).
[55] E. B. Gordon, A. Usenko, and G. Frossati, J. Low Temp. Phys. **130**, 15 (2003).
[56] I. Berent and E. Polturak, Phys. Rev. Lett. **81**, 846 (1998).
[57] I. Berent and E. Polturak, J. Low Temp. Phys. **112**, 337 (1998).
[58] C. Herring, J. Appl. Phys. **21**, 437 (1950).
[59] F. R. N. Nabarro, *Report of a Conference on the Strength of Solids* (Physical Society, London, 1948), p. 75.
[60] P. W. Anderson, Science **324**, 631 (2009).
[61] A. Eyal, O. Pelleg, L. Embon, and E. Polturak, Phys. Rev. Lett. **105**, 025301 (2010).
[62] C. Z. Kwang-Hua, Eur. Phys. J. B **78**, 341 (2010).
[63] S. Rica, Phys. Rev. B **84**, 184535 (2011).
[64] E. T. Swartz and R. O. Pohl, Rev. Mod. Phys. **61**, 605 (1989).
[65] C. Kittel, *Introduction to Solid State Physics* (John Wiley and Sons, New York, 1996).